

Dark Matter at the centre of the Earth

Pau Petit Rosàs

School of Physics and Astronomy

University of Manchester

Jan 2023

Abstract

We present a novel indirect method to search for thermal dark matter particles that scatter with nuclei and annihilate into neutrinos, by modelling how this type of dark matter could be captured by the Sun, the Earth and Jupiter, and generate detectable neutrino fluxes. By comparing these with data from Super Kamiokande and projections from DUNE we set 95% confidence limits on the velocity-averaged annihilation cross-section, which is found to be orders of magnitude smaller than the natural scale for thermal relics. Consequently, we are able to exclude this type of dark matter with masses between 0.01 and 1 GeV and scattering cross-sections of 10^{-31} to 10^{-28} cm 2 , and demonstrate the viability of this method.

1 Introduction

A plethora of cosmological measurements have established that only $\sim 20\%$ of the cold matter in the Universe is baryonic [1, 2, 3]. Despite a range of modified theories of gravity trying to explain this phenomena, none are fully consistent with the data. This suggests that the explanation does not rely on a modification of gravity, but instead, could be ascribed to a non-luminous elusive particle, that hardly ever interacts with standard model (SM) matter. This is generally known as dark matter (DM), and its existence could also contribute to solving apparently unrelated issues in particle physics, such as the hierarchy problem, as most theories devised to explain it also tend to predict new particles. A common denominator between all of these particles is the weak coupling between them and the SM, and they are all included in the umbrella term weakly interactive massive particles (WIMPs).

The search for WIMPs, which has been so far unsuccessful, has spanned over fifty years and has put several bounds on the possible mass and cross-section of this type of DM. The searches can be generally split in direct detection experiments, which hope to detect the nuclear recoils produced by DM interactions, or indirect detection experiments, that try to find the products a thermally-produced DM particle would annihilate into. For these searches, there is a predicted cosmological value for the DM velocity-averaged annihilation cross-section, $\langle \sigma_{an} v \rangle_{NS} \sim 10^{-26} \text{ cm}^3 \text{s}^{-1}$ [4], which can be derived by considering the chemical freeze-out this DM would experience in the Early Universe, and is commonly called the natural scale for thermal relics [5]. Nevertheless, direct and indirect detection approaches face challenges that limit their discovery potential. For instance, in direct detection experiments, detectors work with energy thresholds of a few GeV, and rely on the as-yet to be measured¹ Migdal effect [7]. Furthermore, if the interaction cross-section between DM and SM particles is high enough, the Earth itself would shield the underground experiments from high energy DM particles, as they would scatter and lose energy before reaching the detectors. In indirect detection searches the challenges are more varied, since thermally-produced DM could interact with any SM fermion. The most difficult channel to explore is the neutrino channel, for which the constraints are still a few orders of magnitude away from the natural scale annihilation cross-section $\langle \sigma_{an} v \rangle_{NS}$ [8, 9, 10].

In this report, we propose a new indirect method to set bounds on the annihilation cross-section, for the parameter space where detectors experience Earth shielding effects. This will be done by first simulating how DM is gravitationally captured by our planet, due to the loss of velocity through nuclear scatters, and then setting bounds in its annihilation cross-section by modelling the flux captured DM particles would generate, if they annihilated into neutrinos. Then, by comparing our predictions with measurements from Super-Kamiokande (SK) and projections from DUNE, we hope to set more stringent constraints than the other current methods.

To focus on the range in which Earth shielding limits the results from direct detection experiments, we

¹Although the Migdal effect, also known as electron shakeoff, has not been measured in nuclear scatterings, it has been observed in nuclear decays [6].

select candidates with a scattering cross-section σ_χ between 10^{-25} and 10^{-31} cm 2 , and masses m_χ between 0.01 and 10 GeV. This region, together with the current bounds from different experiments, are also displayed in Fig. 1. In addition, we will extend our method to also include Jupiter and the Sun, bigger bodies that will capture more DM and thus produce bigger theoretical neutrino fluxes, although these will be weaker due to the large distances between production and detection. Nevertheless, they will also allow us to explore a bigger part of the parameter space.

In the following sections, we will first describe how the capture of DM has been modeled and how different factors, such as evaporation or annihilation, have been taken into account. After this discussion we will present how the analysis to set bounds on the annihilation cross-section has been done by using SK data in Section II, and DUNE projections in Section III. In Section IV we present and discuss our results, and we suggest the directions to go with future research and conclude this report in Section V.

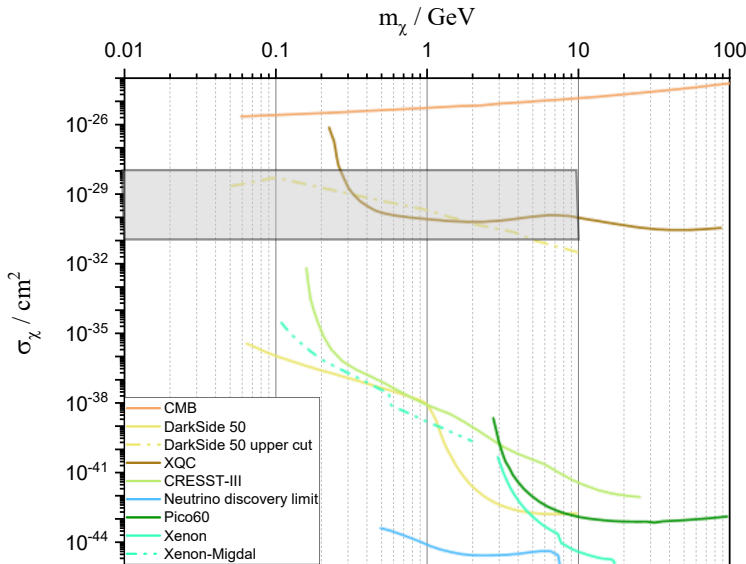


Figure 1: Parameter space for spin independent WIMPs search with excluded regions from experiments including the XQC rocket [11], the CMB SIMP analysis [12], the CRESST-III surface experiment [13], the Xenon with and without considering the Migdal effect [14, 15], the DarkSide 50 collaboration [16], and the Pico-60 bubble chamber [17]. We also include the so-called neutrino floor [18]. The grey highlighted region is the selected parameter space for this work.

2 Theory

In this report, we assume that the population of bounded DM in celestial bodies is affected by three main processes. Firstly, the gravitational capture of the halo DM, characterized by the capture rate \mathcal{C} and the DM particle flux F_χ . Secondly, the annihilation of the DM into neutrinos, denoted by I , the fractional annihilation rate. Finally, the evaporation of the thermalized DM particles, depicted by the fractional

evaporation rate \mathcal{E} . We will explore each of these effects in this order in the following subsections, but it is useful to note beforehand that the number of DM particles inside the bodies N_χ was derived to be

$$\frac{dN_\chi}{dt} = F_\chi \mathcal{C} - N_\chi (\mathcal{E} + I N_\chi). \quad (1)$$

If the capture, evaporation and annihilation rates are assumed to be time-independent Eq. 1 has an analytical solution which we derived, and has the form of,

$$N_\chi(t) = \frac{1}{I} \left[t_{\text{eq}}^{\min} \tanh(t_{\text{eq}}^{\min}(\mathcal{K} + t)) - \frac{\mathcal{E}}{2} \right], \quad (2)$$

$$\mathcal{K} = \frac{1}{t_{\text{eq}}^{\min}} \operatorname{arctanh} \left(\frac{\mathcal{E}}{2t_{\text{eq}}^{\min}} \right), \quad (3)$$

where \mathcal{K} is determined with the initial boundary condition $N_\chi(0) = 0$, and $t_{\text{eq}}^{\min} = \sqrt{\mathcal{E}^2 + 4I F_\chi \mathcal{C}}/2$ is the timescale of this process. Another key timescale to consider is the diffusion timescale, which is defined as the time DM particles take to reach the equilibrium position inside the astronomical objects. This can be estimated as [19]:

$$t_{\text{diff}} = \frac{(\Delta x)^2 n_{SM} \sigma_{\chi,A}}{v_{th}}, \quad (4)$$

where Δx is the radius of the diffusive zone, in our case, the radius of the astronomical object, n_{SM} is the number density of SM nuclei in the zone, $v_{th} = \sqrt{8T(r)/\pi m_\chi}$ is the thermal velocity, and $\sigma_{\chi,A}$ is the cross-section between DM particles and nuclei, defined in Eq. 8. See the following subsections for discussion on the importance of this timescale.

Furthermore, since we are interested in knowing the expected neutrino flux from DM annihilation, it is worth bearing in mind that this is given by

$$F_{\nu\nu} = \frac{IN_\chi^2}{4\pi R^2}, \quad (5)$$

where $F_{\nu\nu}$ is the expected flux and R is the distance to the detector.

2.1 Capture

According to the Standard Halo Model (SHM), the velocity distribution of DM particles in our galaxy is given by a Maxwell-Boltzmann distribution, with a cut-off v_{cut} at the escape velocity of the Milky Way,

$$f(v) \propto \exp \left(-\frac{|v_\chi - \langle v_\chi \rangle|^2}{2\sigma_v^2} \right) \Theta(v_{\text{cut}} - |v_\chi - \langle v_\chi \rangle|), \quad (6)$$

with common values in the literature of $v_{\text{cut}} = 544$ km/s, $\langle v_\chi \rangle = 220$ km/s, and $\sigma_v = \langle v_\chi \rangle / \sqrt{2}$ [20, 21]. Furthermore, this DM distribution intersects with celestial bodies with a flux density of DM particles, determined by the density of the halo, ρ_χ , its mean speed -in the reference frame of the body-, and the mass of the DM particles. This can be expressed as [19]

$$F_\chi = \frac{\rho_\chi \langle v_\chi \rangle}{m_\chi} \sqrt{\frac{8}{3\pi}} \left[1 + \frac{3}{2} \left(\frac{v_{\text{esc}}}{v_\chi} \right)^2 \right], \quad (7)$$

where v_{esc} is the escape velocity of the celestial body, the term in square brackets comes from an enhancement of the flux due to gravitational focusing effects, and $\rho_\chi = 0.3 \text{ GeV c}^{-2} \text{ cm}^{-3}$ from the literature [21].

Because of the coupling between DM and nucleons, the DM flux will interact with the nuclei in the celestial bodies. To model this and go from DM-nucleon cross-section to DM-nucleus cross-section we employ the Born approximation, under the assumption that this interaction is spin and velocity independent and that DM is equally coupled to all nucleons [22]. The approximation is given by

$$\sigma_{\chi,A} = A^2 \left(\frac{\mu(A)}{\mu(N)} \right)^2 \sigma_\chi, \quad (8)$$

where $\mu(x)$ is the reduced mass of DM with x . We bound this cross-section to the geometric cross-section of the nuclei, by taking $\sigma_{\chi,A} = \min(\sigma_{\chi,A}, 4\pi r_N^2)$, where $r_N^2 \approx (1.2 fm)A^{1/3}$.

When DM from the halo scatters with this cross-section through celestial bodies, the velocity distribution is shifted to lower speeds, and a fraction of DM becomes gravitationally bound to the object, since its velocity is smaller than the escape velocity. For the DM in our parameter space, we expect this fraction to be close to unity. This is checked by using Verne [23], and was discussed with more details in the Semester 1 report.

2.1.1 Loss by reflection

Despite the fact that all the DM in our parameter space would be captured in the three bodies of our study, an important part of the flux will be lost by reflection. This effect arises naturally from considering DM particles with a mass smaller or of the order of the mass of SM nuclei present in the astronomical objects since in this case the scattering will be isotropic. As a consequence of the large angles of scattering, some particles will not scatter towards the bodies, and thus will not become bound. We can model this effect by considering a reflection coefficient f_{ref} , which can be analytically computed by considering the total number of scatters required for capture N_{scat} , or equivalently the mean fractional energy lost per scatter β [24],

$$f_{\text{ref}} \approx \frac{2}{\sqrt{\pi N_{\text{scat}}}} = \sqrt{\frac{2}{\pi} \log \left(1 - \frac{1}{2\beta} \right) / \log \left(\frac{v_{\text{esc}}}{v_\chi} \right)}. \quad (9)$$

We can express $\beta = 4m_\chi m_{SM}/(m_\chi + m_{SM})^2$, where m_{SM} is the target nucleus mass. Although the formula is a good approximation for DM particles lighter than 0.1 GeV, it breaks down for heavier particles, when compared to Monte Carlo simulations. This was discussed in the previous report, and the findings are confirmed by recent publications [25]. As a consequence, we decide to employ the results from Monte Carlo simulations, in particular from a modified version of the code **DaMaSCUS** [26]. It is important to note that neither **DaMaSCUS** nor the analytical formula were used for the calculations of the Sun, and the f_{ref} was set to 1. In essence, we assume there is no reflection, as the mean velocity of the DM halo is already smaller than the escape velocity of the Sun.

2.2 Modelling of celestial bodies

For the implementation of **DaMaSCUS** and the calculations for evaporation and annihilation rates in the following subsections it is crucial to have a precise model for the density and temperature profiles of the three celestial bodies, as well as their composition.

For this purpose we use the PREM model [27] for the density of the interior of the Earth, and convert it to temperature using the melting curve of iron [28]. Additionally, we add the effects of the atmosphere using the data from the ISO model [29]. For the composition, we distinguish between atmosphere, crust, mantle and inner core, which are dominated by nitrogen, oxygen and iron respectively. For the Sun, we fit the data from Ref. [30] to a third degree polynomial, and take its composition to be 75% hydrogen and 25% helium. Similarly, we also fit a polynomial to find the density and temperature profiles for Jupiter, using data provided by Ref. [31]. In terms of composition, we distinguish between an outer and an inner envelope, using different percentages for hydrogen and helium, similar to those used for the Sun.

2.3 Annihilation

We model the DM annihilation rate into neutrinos with [32],

$$I = \frac{4\pi}{N_\chi} \int_0^R dr r^2 n_\chi^2 \langle v\sigma \rangle_{ann} = 8\sqrt{2}\pi\sigma_{an} \int_0^R \bar{n}_\chi^2 v_{th} r^2 dr, \quad (10)$$

where n_χ (\bar{n}_χ) is the DM (normalized) number density inside the body, v_{th} is the velocity of the thermalized DM particles, and $\langle v\sigma \rangle_{ann}$ is the velocity-averaged annihilation cross-section. To go from the first to the second equality, we have assumed S-wave annihilation (i.e. annihilation cross-section independent of the velocity), which will be the case throughout the report. A large number of bounds has been set on $\langle v\sigma \rangle_{ann}$ [8, 10, 9], but most of them are still far from the natural scale for thermal relics, and consequently they have not been excluded.

2.4 Evaporation

Captured DM particles will proceed to thermalize and diffuse through the hosting celestial body, and this will cause some of them to gain enough energy to escape the gravitational potential. This effect can be predominant for a large portion of the parameter space, depleting the celestial bodies and making the neutrino flux vanish. For this reason, a proper understanding of it is crucial to make significant and precise bounds on the annihilation cross-section.

The fractional evaporation rate is given by the Jeans formula [24],

$$\mathcal{E} = \frac{3F_{es}}{R\bar{n}_\chi}, \quad (11)$$

where F_{es} is defined using the radius of last scattering surface R_{lss} and the thermal velocity v_{th} ,

$$F_{es} = \frac{n_\chi v_{th}}{2\sqrt{\pi}} \left(1 + \frac{v_{esc}^2}{v_{th}^2} \right) e^{-v_{esc}^2/v_{th}^2} \Big|_{R_{lss}}. \quad (12)$$

To find R_{lss} , we solve [33]:

$$1 = \int_{R_{\text{lss}}}^{\infty} dr \sum_A \sigma_{\chi,A} n_A. \quad (13)$$

As a result of this treatment, knowing the number density distribution of the DM inside the astronomical objects is crucial to find an accurate estimate for the evaporation rate. To find these profiles, we employ the framework developed by Ref. [19],

$$\frac{\nabla n_{\chi}}{n_{\chi}} + (\kappa + 1) \frac{\nabla T}{T} + \frac{m_{\chi} g}{T} = \frac{F_{\chi} R^2}{n_{\chi} D_{\chi} r^2}, \quad (14)$$

where $\kappa \approx -\frac{1}{2}(1 + m_{\chi}/m_{SM})^{-3/2}$ and $D_{\chi} \approx \lambda v_{th}$ are diffusion coefficients, and λ is the mean free path of the DM particles. The left hand side of the equation appears from considering Hydrostatic equilibrium inside the body, as well as assuming DM behaves similarly to an ideal gas. On the other side, the source term arises from the contribution of DM particles that have yet to reach their equilibrium position inside the body. Last semester this right hand side term was dismissed, and the equation was solved using an Runge-Kutta 4 (RK4) routine and normalized using the total number of captured particles. This was a good approximation for Earth in our parameter space, but it no longer works when exploring Jupiter and the Sun. As a consequence, we develop a new method to find a suitable solution: we solve Eq. 14 using an RK4 routine, and we normalize it by using the integrating factor, P ,

$$P = T^{\kappa+1} \exp \left(\int \frac{m_{\chi} g}{T} dr \right), \quad (15)$$

and the constraint that the volume integral of the number density provides the total number of bound DM particles [19]

$$N_{\chi} = 4\pi \int_0^R r^2 n_{\chi} dr. \quad (16)$$

Putting this together, we write the final and normalized solution, $n_{\chi}(r)$,

$$n_{\chi}(r) = n_{\chi}(r)^* + \frac{C}{P(r)}, \quad (17)$$

where $n_{\chi}(r)^*$ is the unnormalized solution from the RK4 routine, and C is a normalization constant determined by the constraining equation. It is important to note that this method has a numerical precision constraint that becomes a problem when N_{χ} is small. In this cases, C can not be found to the required precision, and the normalized population takes negatives values in some points.

We plot how including and dismissing the source term affects the DM distribution in Fig. 2. As previously mentioned, the results are not different for most of our parameter space in the Earth, but this is not the case for Jupiter and the Sun, where the non-equilibrium DM is significant (due to the large amounts of overall capture). In these bodies, the inclusion of the non-equilibrium DM dramatically flattens the distribution at the surface for masses higher than ~ 4 GeV, where the R_{lss} lies, and consequently has a significant effect when calculating \mathcal{E} . A discrepancy between the two solutions is also observed in the small mass range, where DM tends to distribute homogeneously through the object. This discrepancy is not

in the shape of the distributed profile, but on the overall quantity. It is then clear that non-equilibrium DM is significant in the Sun, where large amounts of capture make the non-equilibrium solution (the one with source term) increase the overall population significantly, as opposed to for the Earth or Jupiter.

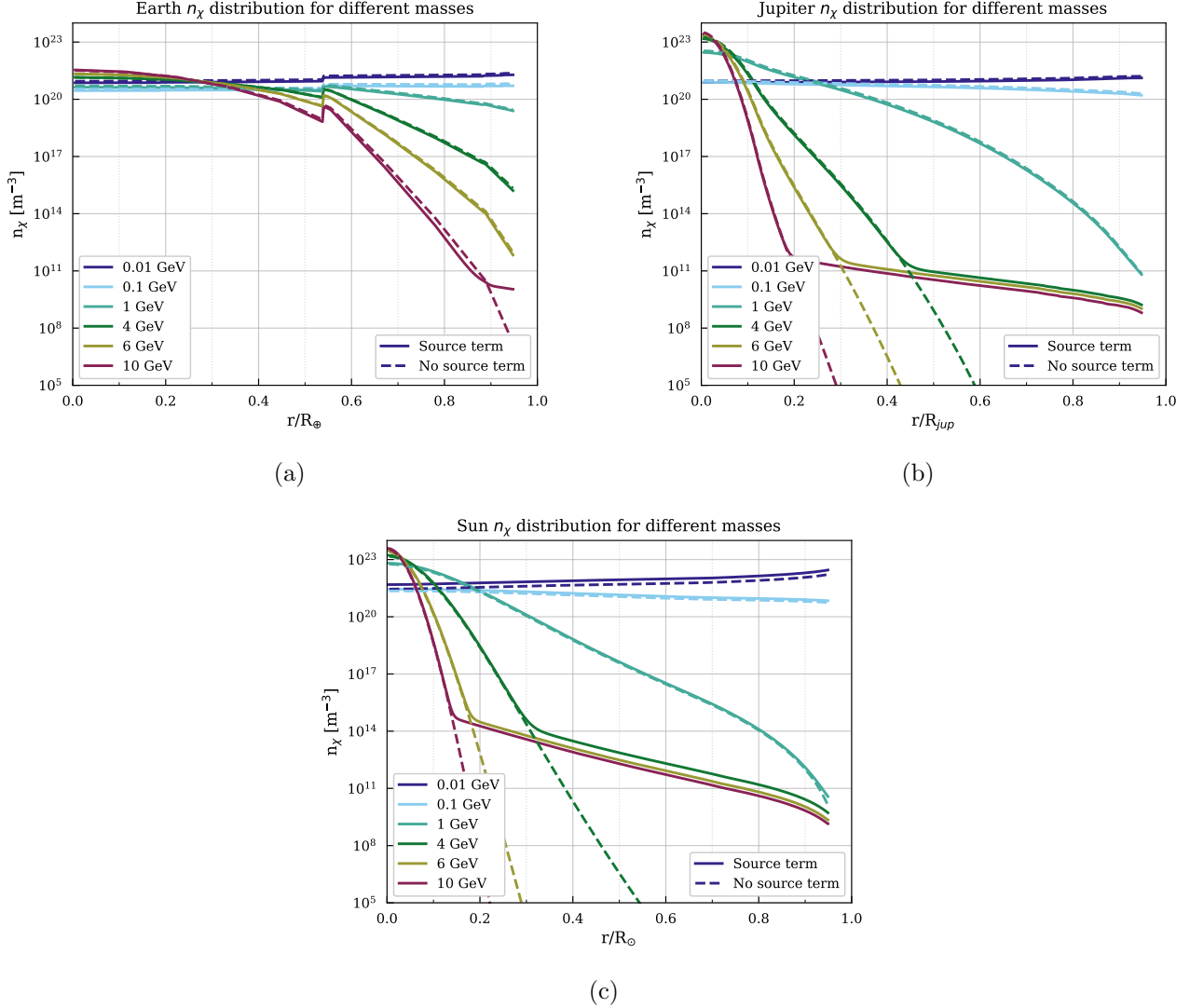


Figure 2: Comparison between DM distributions inside a) Earth, b) Jupiter and c) the Sun with and without including non-equilibrium DM particles. Both solutions converge for masses of the order of 1 GeV, but differ dramatically at the higher masses. A small discrepancy is also observed for small masses in the Sun and Jupiter, see the text for discussion of this effect. Finally, note that the gradient of density and temperature between the crust and the mantle of the Earth generates the bump seen in Sub-figure a) at ~ 0.55 the radius of the Earth.

2.5 Time-dependent Evaporation and Annihilation

Owing to the addition of the source term in Eq. 14, the profiles n_χ become time-dependent, since the normalization condition relies on $N_\chi(t)$. Consequently, if the profiles differ significantly, the evaporation and annihilation rates may not be constant throughout the age of the celestial object. We plot how DM number density profiles change between different times in Fig. 3, where we see that the change is greater the heavier the DM particles are. However, we know that the evaporation rate also diminishes with increasing DM mass. Thus, a change in profile is not significant for these regions.

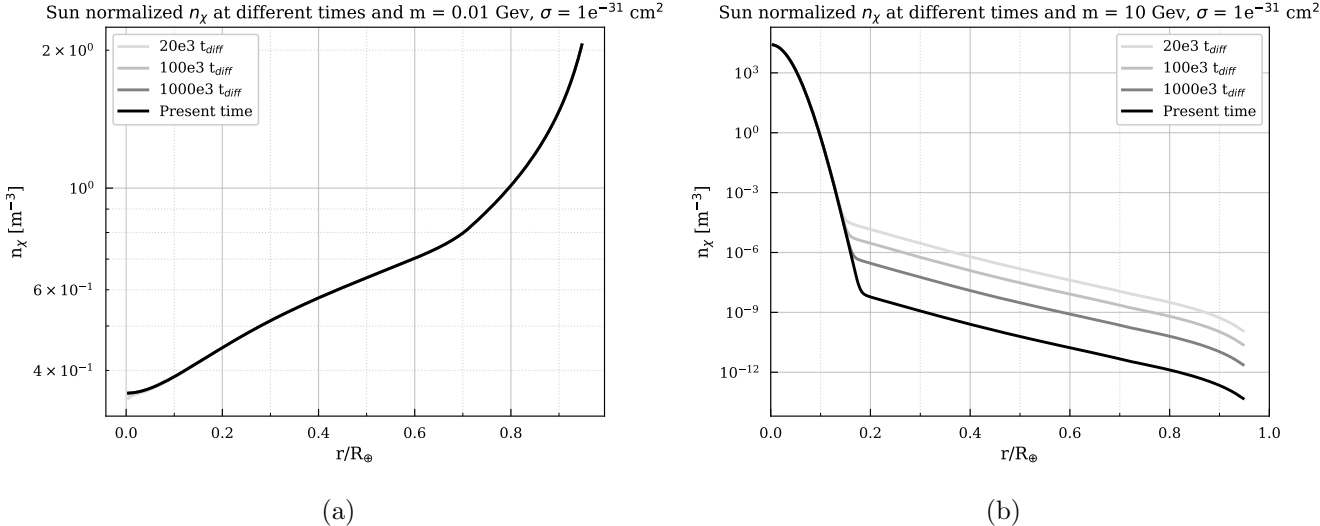


Figure 3: Normalized population distributions along the radius of the Sun for different times (in factors of diffusion timescales) for a benchmark cross-section of 10^{-31} cm^2 and a mass of a) 0.01 GeV and b) 10 GeV . Similar behaviours are observed for the Earth and Jupiter, where the profiles also change more the higher the mass.

There may be an intermediate region where the change in profile is not that significant, but \mathcal{E} is, and thus greatly alters the population. To completely explore this effect, we plot the ratio of evaporation rates at present time and the earliest time we can go in Fig. 4. If the evaporation rate at 1500 diffusion timescales (the lowest we can go without being compromised by the normalization numerical artifact) is the same as the present day for all the parameter space, we can safely assume it to be constant over time. As seen in Fig. 4, this is the case for all the Sun, and almost all the Earth (except a region where the population is depleted anyway), but not for Jupiter, which suggests a numerical time integration should be performed. A second limitation of not solving Eq. 1 taking into account the time-dependence of evaporation and annihilation rates, is that in order to calculate the evaporation and annihilation rates at the present day we have to normalize the population to an N_χ , calculated by assuming no evaporation nor annihilation, which could differ significantly from reality. For these two reasons, we decide to numerically integrate Eq. 1 instead of using Eq. 2 to calculate the present day N_χ .

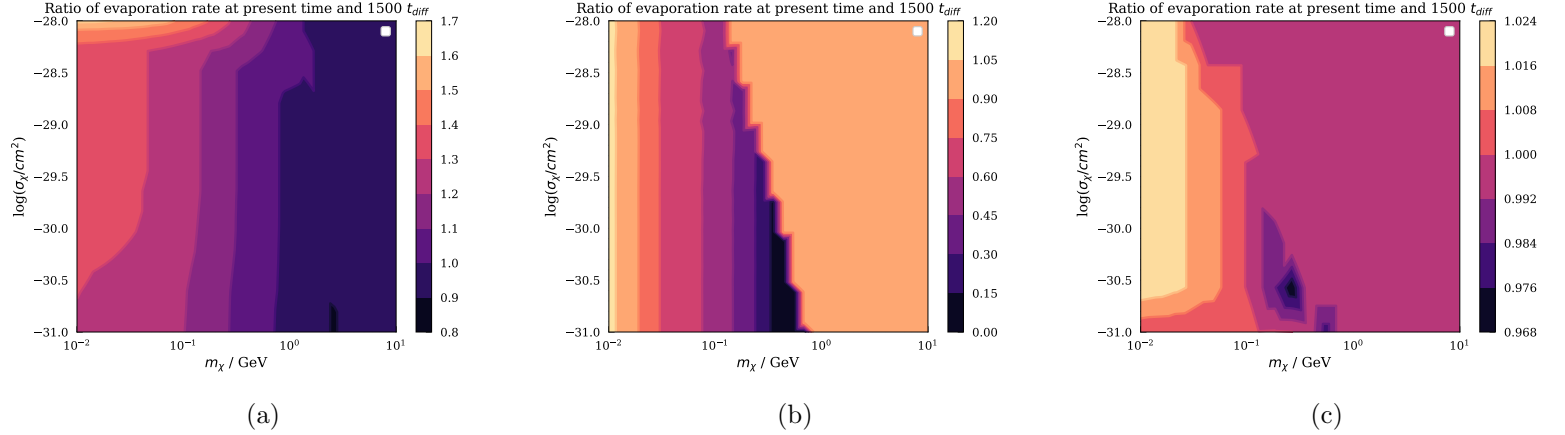


Figure 4: Ratio of evaporation rates at present time and 1500 diffusion timescales in the parameter space for a) Earth, b) Jupiter and c) the Sun. Note the different z-axis.

The method has an important constraint, which derives from the already mentioned precision problem when normalizing the populations distributions n_χ at early times. As a consequence of this limitation, we take the evaporation and annihilation rates to be zero when the population is not normalizable. This is of course non-physical, but does not affect the solution, as seen in Fig. 5. In the regions where evaporation is big the population is quickly depleted, once the population is big enough to normalize the profiles, shown in Fig. 5 a). On the contrary, when evaporation is negligible, it does not affect the linear growth once it kicks in, seen in Fig. 5 c). And finally, when evaporation is not enough to deplete the population but it is significant, it caps the population to a maximum, bringing capture and evaporation to an equilibrium, appreciable in Fig. 5 b).

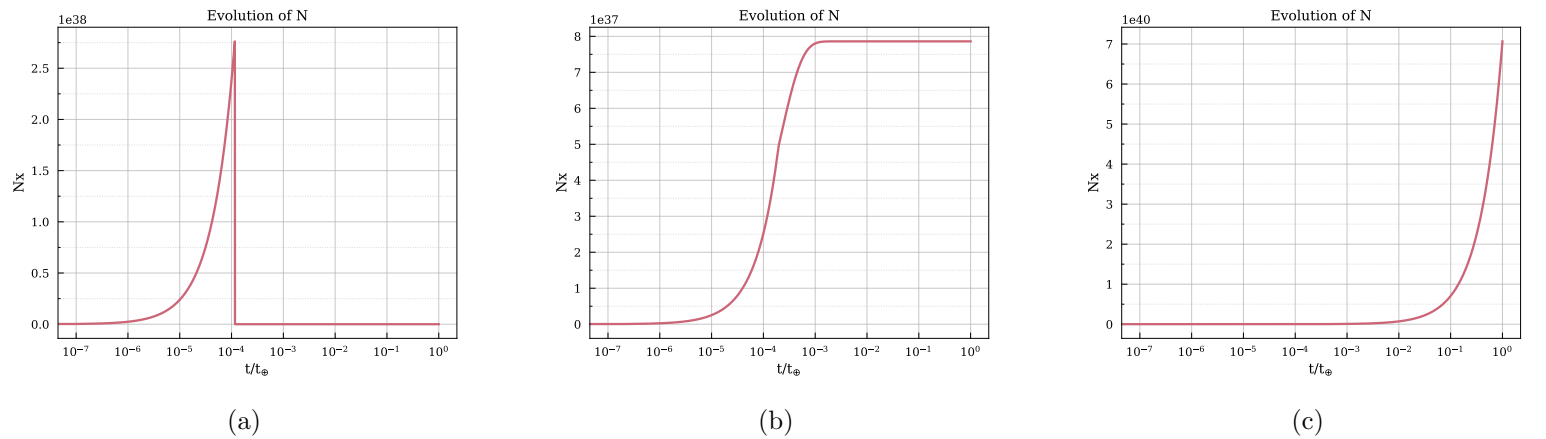


Figure 5: Comparison between behaviour of N_χ over time for different masses, namely for a) $m_\chi = 0.01 \text{ GeV}$, b) $m_\chi = 0.8 \text{ GeV}$ and c) $m_\chi = 10 \text{ GeV}$, taken at $\sigma_\chi = 6 \times 10^{-26} \text{ cm}^2$, $\sigma_{an} = 0 \text{ cm}^2$ and for Earth. Similar behaviours are observed for the Sun and Jupiter. Note logarithmic scale on the time axis.

2.6 Population and Timescales

With this method, we are able to calculate the different present day populations at different annihilation cross-sections. An example is given in Fig. 6, where although the annihilation rate is taken to be zero, we can clearly see that the Sun and Jupiter hold bigger populations than the Earth. Moreover, there are clear regions where evaporation totally dominates and depletes the bodies from DM, but this region is much smaller for Jupiter and the Sun, because although they have higher inner temperatures than the Earth, they compensate with much higher escape velocities, radii and normalized DM populations.

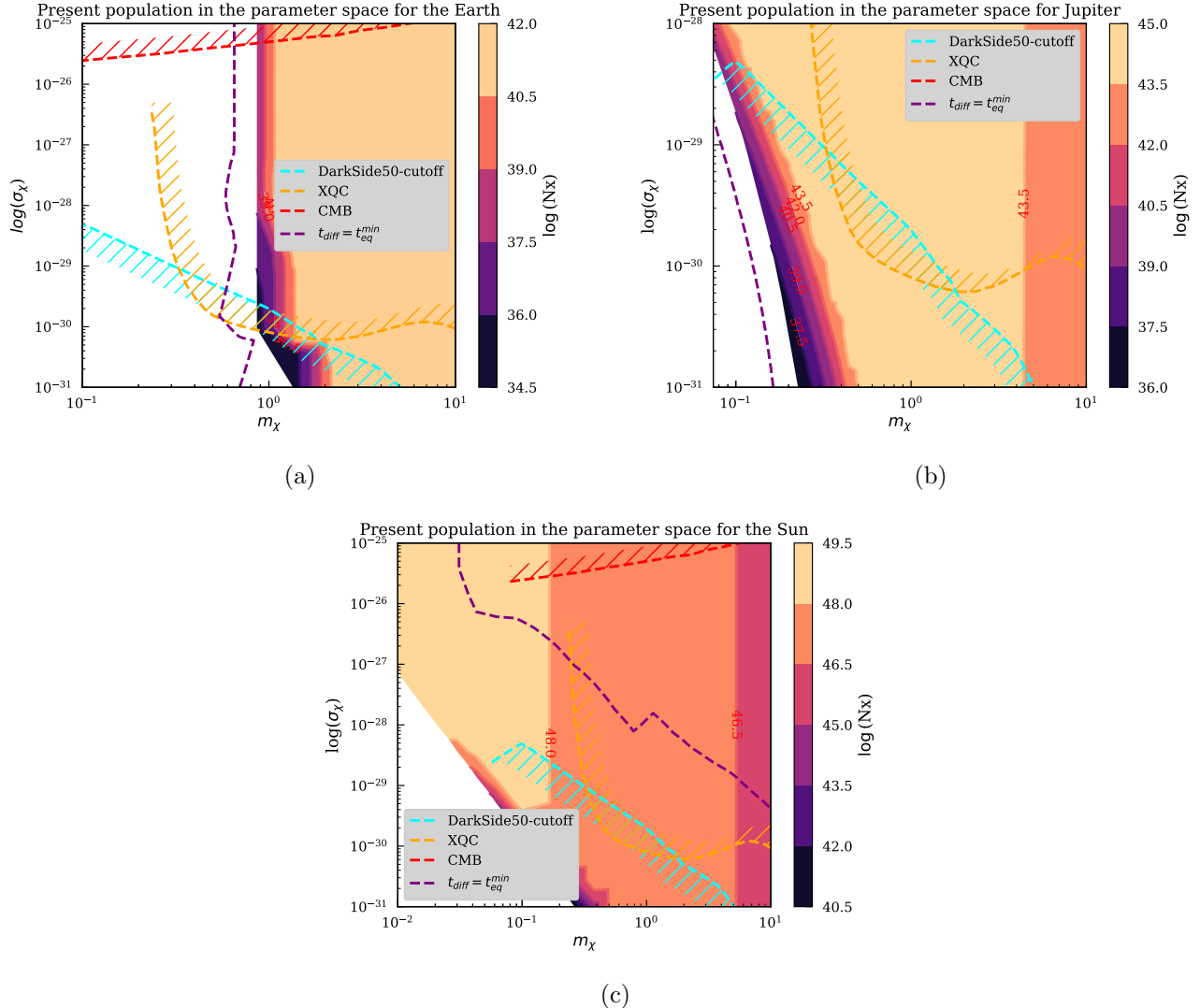


Figure 6: Present day captured DM particles in the mass cross-section parameter space for a) Earth, b) Jupiter and c) the Sun and $\sigma_{an} = 0 \text{ cm}^2$. We also show the appropriate limits from Fig. 1, as well as the contour where the diffusion timescale equals the timescale of the process. Note the different axes.

The dashed purple line in Fig. 6 defines the contour in which the evaporation timescale matches the diffusion timescale. For $t_{\text{eq}}^{\text{min}} < t_{\text{diff}}$ -the region to the left of the dashed line-, our framework is not valid,

since DM will never settle to the calculated positions before evaporating. This is not a concern for the Earth and Jupiter, since the region is depleted anyway by evaporation, but it can be problematic for the Sun, which has more than half the parameter space with $t_{\text{eq}}^{\min} < t_{\text{diff}}$. A new framework, based only on the non-equilibrium population, is needed, but developing it is out of the scope of this work. In addition, in the region where $t_{\text{eq}}^{\min} > t_{\text{diff}}$, the steady distributions could be altered by currents inside the bodies, a phenomena known as advection, which would cause the DM distributions to be homogenized. This is the case only if the advection timescale, t_{adv} , is smaller than the diffusion timescale. This is not the case in our parameter space for Earth, since the advection timescales are of the order of million years, but it is the case for Jupiter if the cross-sections are bigger than 10^{-28} cm^2 , since it has advection timescales of the order of centuries [34, 19]. We thus constrain Jupiter’s parameter space to be between 10^{-28} cm^2 and 10^{-31} cm^2 . In addition, the advection timescale for the Sun goes as low as months. This is generally faster than the diffusion timescale, and thus the results from the Sun have to be taken with the caveat that they may be altered by solar currents. Nevertheless, the convective mixing would homogenize the profiles, making a further boosting of DM abundances plausible.

3 Limits on the annihilation cross-section with Super-Kamiokande

By combining the electron and muon channels from SK I-IV data [35] we constrain the annihilation cross-section in the parameter space, at 95% confidence level, using a likelihood fit [36]. To do so, we consider a plethora of effects, discussed in the following subsections. In this order, we model the signal as seen in the detector and we explore how directionality and correlation can improve our bounds. We also discuss uncertainties on the background models, and errors in our modeled signal.

3.1 The signal in the detector

We first model $\chi\bar{\chi} \rightarrow \nu_l\bar{\nu}_l$ by assuming lepton universality (i.e. DM is equally likely to annihilate into each flavour). Additionally, we take the energy distribution of the neutrinos to be a Dirac delta centered at the mass of the annihilated DM. To transform these true energies to reconstructed energy, we would need to consider three effects, namely the smearing of the energy distribution due to physical interactions, the smearing due to the detector resolution, and neutrino oscillations.

The latter can be dismissed when considering Solar and Jupiter neutrinos, since their baseline are long enough to equalize the percentages of the three neutrino flavours. However, due to matter effects, a full treatment is needed for terrestrial fluxes. We account for this by using the code **GLoBES** [37], which simulates neutrinos oscillations through matter using the PMNS matrix, the generally accepted framework. The results show that DM is either homogeneous enough (at small masses) or with baseline long enough (if it sits at the centre of the Earth, at heavier masses) to make neutrino oscillations not affect the initial flavour distributions. Consequently, we take the ratio of neutrino flavours to be 1:1:1 at the detector independent of celestial body.

In addition, instead of smearing our predicted signal to compare it with SK data, we decide to work with the unfolded spectra from the detector, as presented in Ref. [35].

3.2 Measured flux and background uncertainties

The main neutrino contributor in our mass range are atmospheric neutrinos, which we account for by using the results from HKKM11 [38], HKKM07 [39], FLUKA [40] and Bartol [41], MC simulations based on different flux models. We take HKKM11 to be our reference model and central value, and the uncertainty on the MC simulations to be the maximum and minimum values of the ratios between our HKKM11 and the other models. We show a plot with the data from SK and our reference background model in Fig. 7, for the muon and electron channels. The latter has bigger flux, but the first has less uncertainty on the measurement. We combine both channels to get the most stringent bounds possible.

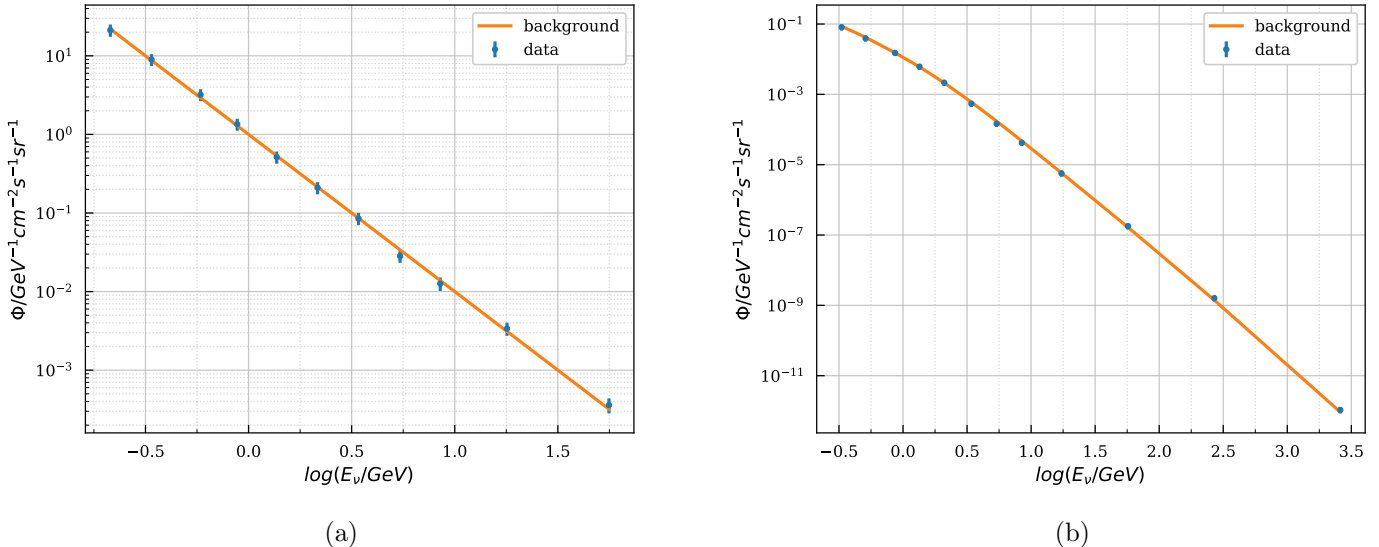


Figure 7: Downwards neutrino fluxes as measured by SK along with the predictions from the background model HKKM11 for the a) electron neutrino and b) muon neutrino channels. Note the flux is divided per steradian and GeV.

The systematic uncertainties on the measured flux by SK are largely dominated by neutrino interactions, and their contribution are followed by the statistical uncertainty. This is due to the poor understanding of the interactions between nuclei and neutrinos, as well as of the few events recorded, common factors in neutrino physics. Furthermore, we also include the detector correlation matrix in our likelihood analysis, which improves our bounds, a result that may be unexpected, but that arises from the fact that our signal is only in one energy bin, and by including the covariant matrix the influence of this bin is extended to others.

Finally, we explore how directionality influences our limit setting. For the Earth the improvement is smaller than an order of magnitude and we decide not to employ it, although implementing it for the Sun and Jupiter can be a future continuation, where we expect it will make a bigger difference.

3.3 Signal Uncertainties

To account for the uncertainties in the modelling of our theoretical flux we include a nuisance parameter in the likelihood code, which takes into account the uncertainty on two SHM parameters, the halo DM density and the mean halo velocity, and one error related to the Jean’s formula, Eq. 12 in this report, for calculating the evaporation rate.

For the uncertainties in the SHM parameters we follow the recommendations in Ref. [21]: we take the variation on the halo density to vary between $0.2 \text{ GeV}^{-2}\text{cm}^{-3}$ and $0.6 \text{ GeV}^{-2}\text{cm}^{-3}$ -the central value recommended being the one stated above, $0.3 \text{ GeV}^{-2}\text{cm}^{-3}$ -, and for the mean halo velocity we use the recommended $\langle v_\chi \rangle = 220 \pm 20 \text{ km/s}$. Finally, we decide to attribute a 50% uncertainty to the Jean’s formula, being this a conservative error based on Ref. [42], where they compare the performance of the formula against MC simulations. This large error is mainly due to the assumption of instant replenishment of the lower end of the velocity distribution when DM particles evaporate, and it could be potentially diminished by calculating evaporation in an alternative way, as suggested, for instance, in Ref. [43]. This was out of the scope of this report.

We find the uncertainty on ρ_χ to be dominant, followed closely by the error on the halo DM mean velocity. The error associated with the fractional evaporation rate is orders of magnitude smaller, but this was to be expected, as evaporation rate is only large for small masses, where the bodies are already depleted of DM population. These errors are added in quadrature, and they can go as high as 300% for the upper errors, and 50% for the lower. It is important to note that the DM density and DM velocity errors will not be included in the likelihood fit, since they are benchmark values for all DM searches. However, the error on evaporation should be included, since it only arises in our method. We will not do so because of time constraints, but the bounds should not vary more than an order of magnitude, since the error is orders of magnitude small than the others.

4 Limits on the annihilation cross-section with DUNE

Using DUNE data projections from Ref. [44] we produce an alternative constraint on the annihilation cross-section, with a similar procedure to the one described for SK. However, some differences arise from the fact that the DUNE detector is still under construction. Mainly, we are forced to work with projections instead of the real data, and as a consequence we can not work with the unfolded spectra. Furthermore, we use a different likelihood code, a modified version of **swordfish** [45], that allows us to work instead of with raw data (which we do not have) with variations on the background, which are added through a nuisance parameter and considered to vary with a Poisson error, independently of each other. Finally, we note that the projected exposure time to obtain this data is 400 kt, which translates to approximately 10 years of data acquisition.

4.1 The Reconstructed Flux

Since we can not work with the unfolded spectra we need to simulate the physical interactions between our flux and the Liquid Argon Time Projection Chamber (LArTPC) of DUNE. We make use of **GENIE** [46], a MC neutrino-nucleus event generator. This is due to time constraints, since in Ref. [44], paper from which we extract the projected data, the alternative **NuWro** [47] software is used. Nevertheless, there is no clear evidence that determines which MC simulation is more accurate, and Ref. [48] finds both software to agree within 20%. The resultant energy distributions can be seen in the dashed line in Fig. 8, in which we have also made the cuts made in the reference paper. In particular, we only select charged currents, mainly dominated by quasi elastic events, which constrains us to only use events with electrons or muons in the final states, and calculate the energy on the calorimeter by taking into account the total energy of the leptons and mesons, as well as the kinetic energy of protons and weird baryons. Neutral pions, which are not seen by DUNE’s LArTPC, are decayed into photons and these are treated like electrons. A summary of the selection cuts for kinetic energy and energy uncertainty for the different particles is presented in Table 1, and obtained from the reference paper. Finally, we apply a Gaussian smearing to the events obtained from **Genie**, simulating the detector resolution. The effect of it can also be seen in the solid line in Fig. 8.

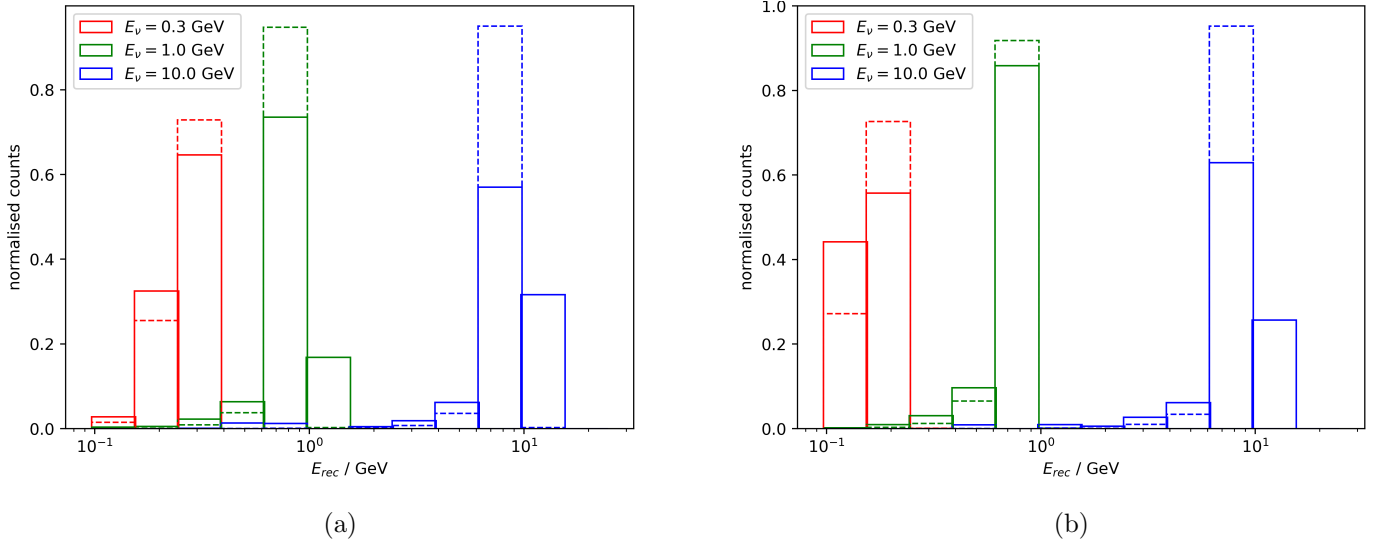


Figure 8: Number of counts for energy bin and different initial energy a) electron neutrinos and b) muon neutrinos comparing the results from **Genie** with (solid) and without (dashed) Gaussian smearing. The analysis is also done for antineutrinos.

5 Results

We present our final results in Fig. 9, where we plot the constraints on the velocity-averaged annihilation cross-section in our parameter space, for every body and for both DUNE and SK analysis. Note that, due to time constraints, we use the results from the time-independent calculations, which should be a really

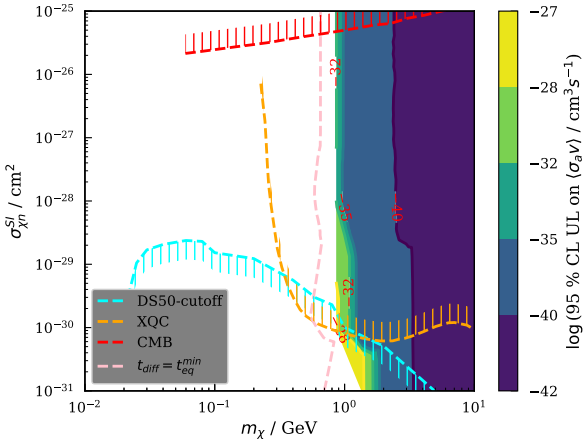
Particle	Minimum K.E. [MeV]	Energy Uncertainty
Proton	30	10%
Pion	30	10%
Λ	30	10%
μ^\pm	5	5%
e^\pm	10	5%

Table 1: Selection cuts and energy uncertainties applied in our analysis, obtained from DUNE Far Detector reconstruction and identification capabilities.

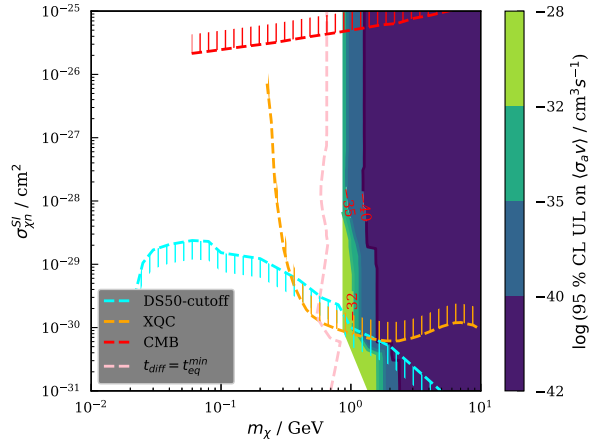
good approximation, especially for the Sun and the Earth, as discussed above in Section 2.5. Nevertheless, we do use the time dependent solutions to determine where the fluxes go to zero, regions that we cut from the x-axes. Additionally, for the Sun and Jupiter, we cut the x-axes at 0.1 GeV, not because the populations die, but because more information is needed for the neutrino backgrounds at lower energies. This is left for future work. In addition, we also cut their y-axis since going to higher cross-sections would make the advection processes dominate, although this is still the case for the Sun as discussed previously. Furthermore, in the same plots we represent the limits in Fig. 1 in red, yellow and blue. Finally, in pink we display the contours where the diffusion timescale matches the process timescale t_{eq}^{\min} , as defined in Section II.

We find that both the SK and DUNE analyses generate bounds orders of magnitude more stringent than the natural scale, which allows us to exclude almost all the parameter space that is not depleted by evaporation. In particular, the Sun and Jupiter allow us to extend the search at smaller masses, but Jupiter is a more reliable body to do so, mainly because of the caveat of the advection timescales in the Sun, but also because of the diffusion timescales, which is seen to dominate in nearly half of the Sun parameter space. In addition, we note that DUNE will be able to set better constraints, with an improvement of around one order of magnitude, and do so consistently for all the parameter space. Nevertheless, we leave as an open question if it would be able to do so in an exposure time lower than ten years, and if so how much time it would take to do.

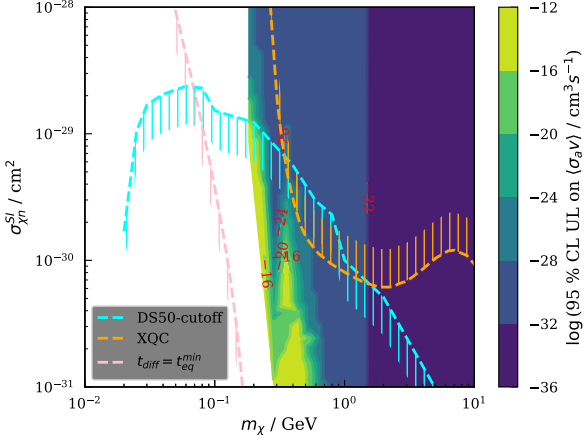
Thanks to the stringent bounds on the velocity-averaged annihilation cross-sections we are able to exclude the studied DM with masses in the range of 0.1 GeV and 10 GeV, as well as scattering cross-sections of 10^{-31} to 10^{-28} cm², mainly relying on the plots from Jupiter. Furthermore, we can exclude higher cross-sections, up to 10^{-25} , using the limits from the Earth but only for masses bigger than 1 GeV. This allows us to reach the limit set by the CMB, which already excludes higher cross-sections. The plots from the Sun could allow us to extend these bounds to lower masses, as seen in Fig 6, but the advection timescale makes developing a new framework crucial for trusting the results. This is left for future work, but should not be arduous, as homogenizing the DM number density profiles should be enough. This would, quite possibly, allow us to fully explore the Earth’s shielded region, although more data from the



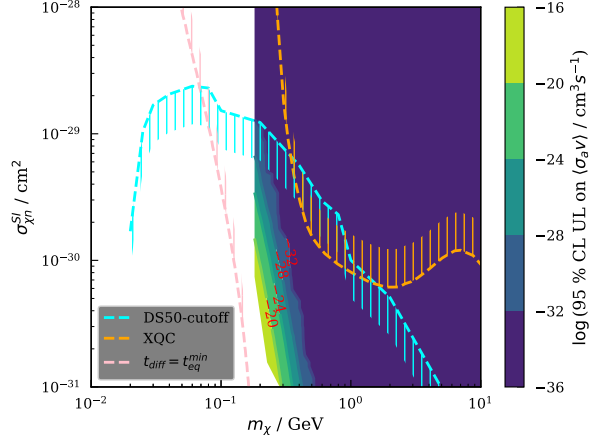
(a) Bounds with Earth and SK analysis



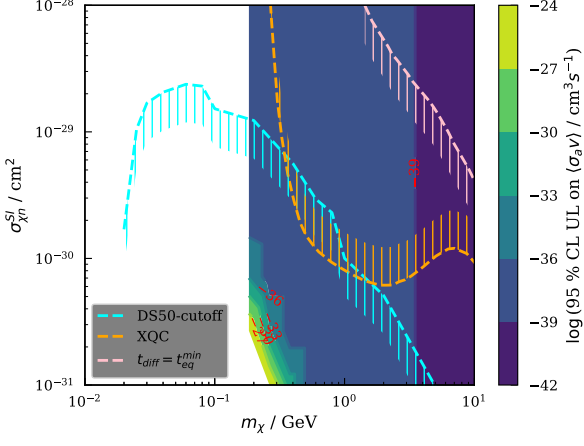
(b) Bounds with Earth and DUNE analysis



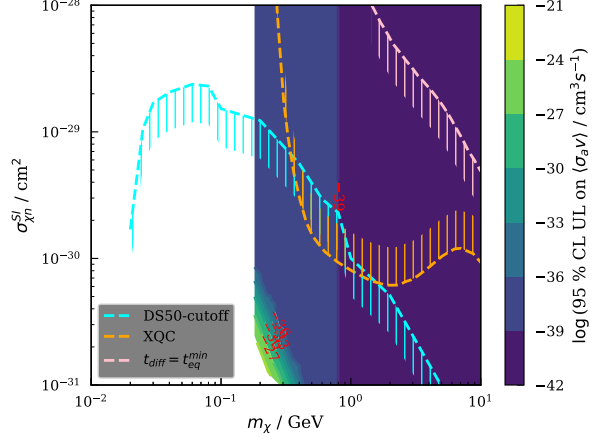
(c) Bounds with Jupiter and SK analysis



(d) Bounds with Jupiter and DUNE analysis



(e) Bounds with the Sun and SK analysis



(f) Bounds with the Sun and DUNE analysis

Figure 9: Bounds on $\langle \sigma_{an} v \rangle$ achieved by our analysis with SK data (left column) and DUNE (right column), for Earth, Jupiter and the Sun. Note the different y-axis for the Earth.

backgrounds at low energies would also be needed. Applying the same would also be possible for Jupiter, but this body would not give better constraints, since his populations are more limited by evaporation than the Sun's.

6 Conclusions

In conclusion, motivated by the challenge of the Earth shielding effects on direct detection experiments and the difficulties of exploring the neutrino channel in indirect detection, we have developed a new method to explore the parameter space of thermal DM, assuming that it scatters with quarks and annihilates into neutrinos. By modelling how this type of DM would be captured by celestial bodies and generate neutrino fluxes, we have been able to exclude a big region of the studied parameter space, using data from Super Kamiokande and projections from DUNE, and we have shown that the framework can also be applied to different celestial bodies.

The constraints on the velocity-averaged annihilation cross-section are orders of magnitude better than the natural scale and previous searches at these masses, which is to be expected, since we are applying another constraint to the DM (which is that it interacts with quarks). We have thus been able to exclude this type of DM with masses in the range of 0.1 GeV and 10 GeV, as well as scattering cross-sections of 10^{-31} to 10^{-28} cm². Furthermore, we have shown that if the advective currents of the Sun were to be included in our framework, we could also exclude a big portion of the Earth shielded regions, which have not been constrained to this date. Nevertheless, we also note that it would be challenging to make this method work at other parameter-spaces, since at lower masses the evaporation depletes the bodies and no flux is generated, and at lower scattering cross-sections capture is strongly reduced. In addition, the dominant source of error is, like in other DM searches, our understanding of the DM halo, but in this case we are also constrained by the calculation of the evaporation rate. Experimentally, we are also bound by the systematic and statistical uncertainties of the detectors, but also of the backgrounds, for which we need data at lower masses.

Possible extensions of the work include studying how would the results vary for different types of annihilation, like assuming the DM is also able to decay into quarks, as well as modelling other types of interactions between DM and nuclei (spin-dependent, different coupling to different nucleons, ...). This would make our conclusions less model dependent, and potentially give other constraining results.

References

- [1] Vera C. Rubin and Jr. Ford W. Kent. “Rotation of the Andromeda Nebula from a Spectroscopic Survey of Emission Regions”. In: *Astrophysical Journal* 159 (Feb. 1970), p. 379. DOI: 10.1086/150317.
- [2] S. M. Faber and R. E. Jackson. “Velocity dispersions and mass-to-light ratios for elliptical galaxies.” In: *Astrophysical Journal* 204 (Mar. 1976), pp. 668–683. DOI: 10.1086/154215.

- [3] Priyamvada Natarajan et al. “Mapping substructure in the HST Frontier Fields cluster lenses and in cosmological simulations”. In: *Monthly Notices of the Royal Astronomical Society* 468.2 (Feb. 2017), pp. 1962–1980. DOI: [10.1093/mnras/stw3385](https://doi.org/10.1093/mnras/stw3385).
- [4] Gary Steigman, Basudeb Dasgupta, and John F. Beacom. “Precise relic WIMP abundance and its impact on searches for dark matter annihilation”. In: *Physical Review D* 86.2 (July 2012). DOI: [10.1103/physrevd.86.023506](https://doi.org/10.1103/physrevd.86.023506).
- [5] Howard Baer et al. “Dark matter production in the early Universe: Beyond the thermal WIMP paradigm”. In: *Physics Reports* 555 (Feb. 2015), pp. 1–60. DOI: [10.1016/j.physrep.2014.10.002](https://doi.org/10.1016/j.physrep.2014.10.002).
- [6] X. Fabian et al. “Electron shakeoff following the β^+ decay of $^{19}\text{Ne}^+$ and $^{35}\text{Ar}^+$ trapped ions”. In: *Phys. Rev. A* 97 (2 Feb. 2018), p. 023402. DOI: [10.1103/PhysRevA.97.023402](https://doi.org/10.1103/PhysRevA.97.023402).
- [7] H.M. Araújo et al. “The MIGDAL experiment: Measuring a rare atomic process to aid the search for dark matter”. In: *Astroparticle Physics* 151 (Sept. 2023), p. 102853. DOI: [10.1016/j.astropartphys.2023.102853](https://doi.org/10.1016/j.astropartphys.2023.102853).
- [8] John F. Beacom, Nicole F. Bell, and Gregory D. Mack. “Upper Bound on the Dark Matter Total Annihilation Cross Section”. In: *Physical Review Letters* 99.23 (Dec. 2007). DOI: [10.1103/physrevlett.99.231301](https://doi.org/10.1103/physrevlett.99.231301).
- [9] David McKeen et al. *Dark Matter Annihilation Inside Large Volume Neutrino Detectors*. 2023. arXiv: 2303.03416 [hep-ph].
- [10] M. Blennow et al. “Neutrino portals to dark matter”. In: *The European Physical Journal C* 79.7 (July 2019). DOI: [10.1140/epjc/s10052-019-7060-5](https://doi.org/10.1140/epjc/s10052-019-7060-5).
- [11] Adrienne L. Erickcek et al. “Constraints on the interactions between dark matter and baryons from the x-ray quantum calorimetry experiment”. In: *Physical Review D* 76.4 (Aug. 2007). DOI: [10.1103/physrevd.76.042007](https://doi.org/10.1103/physrevd.76.042007).
- [12] Vera Gluscevic and Kimberly K. Boddy. “Constraints on Scattering of keV–TeV Dark Matter with Protons in the Early Universe”. In: *Physical Review Letters* 121.8 (Aug. 2018). DOI: [10.1103/physrevlett.121.081301](https://doi.org/10.1103/physrevlett.121.081301).
- [13] Jonathan H. Davis. “Probing Sub-GeV Mass Strongly Interacting Dark Matter with a Low-Threshold Surface Experiment”. In: *Phys. Rev. Lett.* 119 (21 Nov. 2017), p. 211302. DOI: [10.1103/PhysRevLett.119.211302](https://doi.org/10.1103/PhysRevLett.119.211302).
- [14] E. Aprile *et. al.* “Constraining the Spin-Dependent WIMP-Nucleon Cross Sections with XENON1T”. In: *Physical Review Letters* 122.14 (Apr. 2019). DOI: [10.1103/physrevlett.122.141301](https://doi.org/10.1103/physrevlett.122.141301).
- [15] E. Aprile *et. al.* “Dark Matter Search Results from a One Ton-Year Exposure of XENON1T”. In: *Physical Review Letters* 121.11 (Sept. 2018). DOI: [10.1103/physrevlett.121.111302](https://doi.org/10.1103/physrevlett.121.111302).
- [16] P. Agnes *et. al.* “Low-Mass Dark Matter Search with the DarkSide-50 Experiment”. In: *Physical Review Letters* 121.8 (Aug. 2018). DOI: [10.1103/physrevlett.121.081307](https://doi.org/10.1103/physrevlett.121.081307).
- [17] C. Amole *et. al.* “Dark matter search results from the complete exposure of the PICO-60 bubble chamber”. In: *Physical Review D* 100.2 (July 2019). DOI: [10.1103/physrevd.100.022001](https://doi.org/10.1103/physrevd.100.022001).

- [18] J. Billard, E. Figueira-Feliciano, and L. Strigari. “Implication of neutrino backgrounds on the reach of next generation dark matter direct detection experiments”. In: *Phys. Rev. D* 89 (2 Jan. 2014), p. 023524. DOI: 10.1103/PhysRevD.89.023524.
- [19] Rebecca K. Leane and Juri Smirnov. *Floating Dark Matter in Celestial Bodies*. 2022. arXiv: 2209.09834 [hep-ph].
- [20] T. Piffl et al. “The RAVE survey: the Galactic escape speed and the mass of the Milky Way”. In: *Astronomy & Astrophysics* 562 (Feb. 2014), A91. DOI: 10.1051/0004-6361/201322531.
- [21] D. Baxter et al. “Recommended conventions for reporting results from direct dark matter searches”. In: *The European Physical Journal C* 81.10 (Oct. 2021). DOI: 10.1140/epjc/s10052-021-09655-y.
- [22] Matthew C. Digman et al. “Not as big as a barn: Upper bounds on dark matter-nucleus cross sections”. In: *Physical Review D* 100.6 (Sept. 2019). DOI: 10.1103/physrevd.100.063013.
- [23] Bradley J. Kavanagh. “Earth scattering of superheavy dark matter: Updated constraints from detectors old and new”. In: *Physical Review D* 97.12 (June 2018). DOI: 10.1103/physrevd.97.123013.
- [24] David A. Neufeld, Glennys R. Farrar, and Christopher F. McKee. “Dark Matter that Interacts with Baryons: Density Distribution within the Earth and New Constraints on the Interaction Cross-section”. In: *Astrophysical Journal* 866.2, 111 (Oct. 2018), p. 111. DOI: 10.3847/1538-4357/aad6a4.
- [25] Joseph Bramante et al. *Light Dark Matter Accumulating in Terrestrial Planets: Nuclear Scattering*. 2022. arXiv: 2210.01812 [hep-ph].
- [26] Timon Emken and Chris Kouvaris. “DaMaSCUS: the impact of underground scatterings on direct detection of light dark matter”. In: *Journal of Cosmology and Astroparticle Physics* 2017.10 (Oct. 2017), pp. 031–031. DOI: 10.1088/1475-7516/2017/10/031.
- [27] A. M. Dziewonski and D. L. Anderson. “Preliminary reference earth model”. In: *Phys. Earth Planet. Interiors* 25 (1981), pp. 297–356. DOI: 10.1016/0031-9201(81)90046-7.
- [28] S. Anzellini et al. “Melting of Iron at Earth’s Inner Core Boundary Based on Fast X-ray Diffraction”. In: *Science* 340.6131 (2013), pp. 464–466. DOI: 10.1126/science.1233514.
- [29] International Organization for Standardization. “Standard Atmosphere”, ”ISO: 2533:1975”. In: (2021).
- [30] John N. Bahcall, M. H. Pinsonneault, and G. J. Wasserburg. “Solar models with helium and heavy-element diffusion”. In: *Rev. Mod. Phys.* 67 (4 Oct. 1995), pp. 781–808. DOI: 10.1103/RevModPhys.67.781.
- [31] Martin French et al. “Ab Initio Simulations for Material Properties along the Jupiter Adiabat”. In: *The Astrophysical Journal Supplement Series* 202 (Sept. 2012), p. 5. DOI: 10.1088/0067-0049/202/1/5.
- [32] Maxim Pospelov and Harikrishnan Ramani. “Earth-bound millicharge relics”. In: *Physical Review D* 103.11 (June 2021). DOI: 10.1103/physrevd.103.115031.

- [33] D. McKeen *et. al.* “Accelerating Earth-bound dark matter”. In: *Phys. Rev. D* 106 (2022). doi: <https://doi.org/10.1103/PhysRevD.106.035011>.
- [34] F.J.P. Soler, C.D. Froggatt, and F. Muheim. “*Neutrinos in particle physics, astrophysics and cosmology*”. 2009. doi: 10.1007/978-3-642-17560-2.
- [35] E. Richard *et. al.* “Measurements of the atmospheric neutrino flux by Super-Kamiokande: Energy spectra, geomagnetic effects, and solar modulation”. In: *Physical Review D* 94.5 (Sept. 2016). doi: 10.1103/physrevd.94.052001.
- [36] Glen Cowan et al. “Asymptotic formulae for likelihood-based tests of new physics”. In: *The European Physical Journal C* 71.2 (Feb. 2011). doi: 10.1140/epjc/s10052-011-1554-0.
- [37] P. Huber, M. Lindner, and W. Winter. “Simulation of long-baseline neutrino oscillation experiments with GLoBES”. In: *Computer Physics Communications* 167.3 (May 2005), pp. 195–202. doi: 10.1016/j.cpc.2005.01.003.
- [38] M. Honda et al. “Improvement of low energy atmospheric neutrino flux calculation using the JAM nuclear interaction model”. In: *Phys. Rev. D* 83 (12 June 2011), p. 123001. doi: 10.1103/PhysRevD.83.123001.
- [39] M. Honda et al. “Calculation of atmospheric neutrino flux using the interaction model calibrated with atmospheric muon data”. In: *Phys. Rev. D* 75 (4 Feb. 2007), p. 043006. doi: 10.1103/PhysRevD.75.043006.
- [40] G. Battistoni et al. “The FLUKA atmospheric neutrino flux calculation”. In: *Astroparticle Physics* 19.2 (May 2003), pp. 269–290. doi: 10.1016/s0927-6505(02)00246-3.
- [41] G. D. Barr et al. “Three-dimensional calculation of atmospheric neutrinos”. In: *Phys. Rev. D* 70 (2 July 2004), p. 023006. doi: 10.1103/PhysRevD.70.023006.
- [42] J. -Y. Chaufray. “Departure of the thermal escape rate from the jeans escape rate for atomic hydrogen at Earth, Mars, and Pluto”. In: 198, 105178 (Apr. 2021), p. 105178. doi: 10.1016/j.pss.2021.105178.
- [43] Andrew Gould. “Weakly Interacting Massive Particle Distribution in and Evaporation from the Sun”. In: *Astrophysical Journal* 321 (Oct. 1987), p. 560. doi: 10.1086/165652.
- [44] Kevin J. Kelly et al. “DUNE atmospheric neutrinos: Earth tomography”. In: *Journal of High Energy Physics* 2022.5 (May 2022). doi: 10.1007/jhep05(2022)187.
- [45] Thomas D. P. Edwards and Christoph Weniger. *swordfish: Efficient Forecasting of New Physics Searches without Monte Carlo*. 2017. arXiv: 1712.05401 [hep-ph].
- [46] Costas Andreopoulos et al. *The GENIE Neutrino Monte Carlo Generator: Physics and User Manual*. 2015. arXiv: 1510.05494 [hep-ph].
- [47] J. Ź muda et al. “NuWro Monte Carlo Generator of Neutrino Interactions - First Electron Scattering Results”. In: *Acta Physica Polonica B* 46.11 (2015), p. 2329. doi: 10.5506/aphyspolb.46.2329.

- [48] Carsten Rott et al. “Directional searches at DUNE for sub-GeV monoenergetic neutrinos arising from dark matter annihilation in the Sun”. In: *Journal of Cosmology and Astroparticle Physics* 2017.01 (Jan. 2017), pp. 016–016. doi: 10.1088/1475-7516/2017/01/016.